Nanoscale Advances

ROYAL SOCIETY OF CHEMISTRY

PAPER

View Article Online
View Journal

Cite this: DOI: 10.1039/d6na00120c

DFT investigation of Na-ion interaction with Janus 1T-HfSTe monolayer for sodium-ion battery anodes

Khang D. Pham,[ab] Duc-Quang Hoang,[c] Hien D. Tong,[d] Thi H. Ho[ef] and Tuan V. Vu[*ef]

Developing high-performance anode materials with efficient and stable Na-ion storage capability and fast ion-transport kinetics remains a key challenge for advancing sodium-ion batteries. In this work, density functional theory calculations are employed to systematically investigate the Janus HfSTe monolayer as a potential anode material for sodium-ion batteries. The results indicate that the HfSTe monolayer possesses intrinsic metallic conductivity together with good mechanical, thermal, and dynamical stability. CI-NEB calculations reveal low Na diffusion barriers, with a minimum value of 0.18 eV, suggesting favorable Na-ion transport kinetics. Upon progressive sodiation, Na storage proceeds *via* a layer-by-layer adsorption mechanism, delivering a high theoretical capacity of 554.8 mAh g^{-1} and a relatively low average open-circuit voltage of 0.33 V, which is suitable for anode operation. Notably, the HfSTe monolayer maintains its metallic character even at high sodiation levels, accompanied by a moderate volume expansion of 10.55%. These results highlight the Janus HfSTe monolayer as a promising anode candidate for high-performance sodium-ion batteries.

Received 14th February 2026
Accepted 23rd May 2026

DOI: 10.1039/d6na00120c

rsc.li/nanoscale-advances

1 Introduction

The demand for high-performance and sustainable energy storage systems has become a central challenge in modern science and technology, particularly in the context of the rapid expansion of renewable energy sources and the ongoing electrification of various application sectors.[1,2] Lithium-ion batteries (LIBs) continue to play a dominant role in energy storage technologies owing to their high energy density and well-established reliability.[3,4] However, concerns associated with lithium resource limitations and long-term scalability have stimulated growing interest in alternative battery technologies.[5–7] In this context, sodium-ion batteries (SIBs) have attracted significant interest as an alternative energy storage system due to the natural abundance and wide availability of sodium, which makes them particularly suitable for large-scale applications.[8,9]

Nevertheless, the electrochemical performance of SIBs is strongly governed by the choice of electrode materials, among which the anode plays a critical role. Graphite, the standard anode material for lithium-ion batteries (LIBs), exhibits very limited Na^+ storage capability (with a theoretical capacity of only ~35 mAh g^{-1})[10] because the ionic radius of sodium (1.02 Å) is significantly larger than that of lithium (0.76 Å),[11] leading to geometric and thermodynamic incompatibility with the intercalation galleries of the graphite structure. As a consequence, weak Na^+ affinity and sluggish intercalation kinetics result in low storage capacity and poor cycling stability. Therefore, the development of new anode materials capable of strong Na adsorption, fast diffusion, and the retention of high electrical conductivity and structural stability throughout repeated sodiation/desodiation processes is regarded as a key requirement for enhancing the performance of sodium-ion batteries.[8,12–14]

In recent years, two-dimensional (2D) materials have attracted considerable attention as prospective anode materials for SIBs, owing to their high specific surface area, adaptable layered architectures, and tunable electronic characteristics.[15,16] Among them, 2D Janus structures, in which the two sides of a monolayer are terminated by different chemical elements, have emerged as a promising platform for electrode design.[13,17–21] Owing to the broken out-of-plane mirror symmetry, Janus monolayers exhibit an asymmetric charge

[a]Institute of Research and Development, Duy Tan University, Da Nang 550000, Vietnam. E-mail: phamdinhkhang@duytan.edu.vn
[b]School of Engineering & Technology, Duy Tan University, Da Nang 550000, Vietnam
[c]Faculty of Applied Sciences, HCMC University of Technology & Engineering, 01 Vo Van Ngan, Thu Duc, Ho Chi Minh City 700000, Vietnam
[d]Faculty of Engineering, Vietnamese-German University (VGU), Ring Road 4, Quarter 4, Thoi Hoa Ward, Ho Chi Minh City, Vietnam
[e]Laboratory for Computational Physics, Institute for Computational Science and Artificial Intelligence, Van Lang University, Ho Chi Minh City, Vietnam. E-mail: tuan.vu@vlu.edu.vn
[f]Faculty of Mechanical, Electrical, and Computer Engineering, Van Lang School of Technology, Van Lang University, Ho Chi Minh City, Vietnam

distribution across the two surfaces, which can induce an intrinsic dipole moment and a built-in electrostatic field.[17–19,22–24] This asymmetric electrostatic environment can modulate ion adsorption strength, site preference, and diffusion pathways, thereby providing an additional route to tune ion-storage and ion-transport properties in two-dimensional systems.[25–28] First-principles studies have demonstrated that 2D Janus materials constitute a promising class of anode candidates for sodium-ion batteries (SIBs), owing to their favorable Na adsorption energetics, fast in-plane ion diffusion, and suitable electrochemical characteristics. Ahmad *et al.*[28] reported that Na adsorption on the Janus WSSe monolayer is energetically stable and can induce a semiconductor-to-metal transition, resulting in improved electronic conductivity, a low open-circuit voltage (OCV) of about 0.57 V, and a theoretical Na-storage capacity of 371.5 mAh g^{-1}, together with a low in-plane Na diffusion barrier of 0.07 eV on the Se-terminated surface. Similar behavior was observed in Janus MoSSe, which exhibits a high Na-storage capacity of 510 mAh g^{-1} and an ultralow Na diffusion barrier of 0.075 eV, indicating favorable Na-ion transport kinetics.[29] Beyond Janus systems, the BP_3 monolayer has also been identified as a promising SIB anode owing to its high Na-storage capacity and rapid Na-ion diffusion.[30] In addition, Janus BeSeCl monolayer has been predicted to deliver even higher Na-storage capacities (699 mAh g^{-1}) with low diffusion barriers and low OCVs, further underscoring the versatility of Janus chemistry in tuning ion-storage performance.[31] Collectively, these studies suggest that the intrinsic out-of-plane asymmetry of Janus monolayers creates differentiated surface environments that are conducive to stable Na adsorption, fast in-plane ion diffusion, and low operating voltages, making them promising anode candidates for sodium-ion batteries.

Recently, Hf-based Janus chalcogenides, particularly the 1T-HfSTe monolayer, have emerged as an interesting class of two-dimensional materials owing to their distinctive structural, mechanical, and electronic properties. Previous studies on related Janus Hf systems have mainly focused on their structural stability and electronic/optoelectronic features, including the stability and electronic properties of Janus HfSSe and its partially oxygenated counterparts.[32] More recently, the 1T-HfSTe monolayer itself has been investigated in terms of its possible atomic configurations, dynamical stability, intrinsic metallicity, and surface asymmetry.[33] Previous reports have also suggested that Janus HfSTe possesses relatively low in-plane stiffness, which may facilitate the accommodation of structural deformation during ion adsorption, while its metallic character is favorable for electron transport in electrode applications.[21,34] Moreover, HfSTe-containing Janus-embedded superlattices have been explored for thermoelectric applications, further indicating the potential multifunctionality of this family of materials.[35] These characteristics make Janus 1T-HfSTe a potentially attractive candidate for energy-storage-related applications. Nevertheless, to date, the Na-storage behavior of the pristine Janus 1T-HfSTe monolayer has not been systematically clarified. In particular, several key descriptors governing anode performance remain unclear, including: (i) the preferred Na adsorption sites and binding energies on the asymmetric surfaces; (ii) the diffusion pathways and corresponding migration barriers that determine charge/discharge kinetics; (iii) the maximum theoretical storage capacity and the evolution of the open-circuit voltage (OCV) with Na concentration; and (iv) the preservation of metallic conductivity at different sodiation levels. Addressing these issues requires an atomistic-level approach, for which first-principles calculations can provide quantitative insights that remain difficult to obtain directly from current experiments.

In this work, we carry out a comprehensive density functional theory investigation of the interactions between Na ions and the Janus 1T-HfSTe monolayer. The study focuses on identifying energetically favorable Na adsorption sites and adsorption energies, exploring in-plane Na diffusion pathways and the associated energy barriers, estimating the theoretical Na storage capacity and the open-circuit voltage profile, as well as analyzing the evolution of the electronic structure through band structure and density-of-states calculations during the sodiation process. In addition, the structural response of the Janus HfSTe monolayer upon progressive Na insertion is examined by evaluating the volume expansion induced by sodiation. The obtained results are expected to provide fundamental and quantitative insights into Na storage mechanisms in Janus two-dimensional materials, thereby elucidating the potential of the Janus 1T-HfSTe monolayer as an anode material for sodium-ion batteries from an atomic-scale materials design perspective.

2 Computational details

First-principles calculations were performed within the density functional theory (DFT) formalism employing the projector augmented-wave (PAW) approach, as implemented in the Vienna *ab initio* Simulation Package (VASP).[36,37] The exchange–correlation effects were treated using the Perdew–Burke–Ernzerhof (PBE) form of the generalized gradient approximation (GGA), with long-range dispersion interactions accounted for through the DFT-D3 method incorporating Becke–Johnson damping.[38] A kinetic-energy cutoff of 550 eV was adopted for the plane-wave basis set. Electronic and ionic relaxations were considered converged when the total energy difference was below 10^{-6} eV and the residual atomic forces were less than 0.01 eV $Å^{-1}$.

The Janus 1T-HfSTe monolayer was first constructed at the primitive-cell level and fully optimized. The optimized primitive structure was then expanded into a 3×3 in-plane supercell for the adsorption, diffusion, and sodiation calculations. A vacuum layer exceeding 15 Å was applied along the direction perpendicular to the monolayer to suppress interactions between periodic images. Considering the out-of-plane asymmetry inherent to the Janus configuration, dipole corrections were introduced along the vertical direction. Brillouin zone integrations were carried out using a Γ-centered $5 \times 5 \times 1$ Monkhorst–Pack *k*-point grid for the supercell calculations.[39] The adequacy of this *k*-point sampling was further verified by convergence tests, as provided in the SI. The elastic constants were derived from the calculated strain–stress relationships, while the

projected band structures and related post-processing analyses were performed with the aid of the VASPKIT package.[40]

To examine thermal stability, *ab initio* molecular dynamics (AIMD) simulations were performed in the canonical (NVT) ensemble using the Nosé–Hoover thermostat.[41,42] A 3 × 3 × 1 supercell was adopted, and each AIMD run was carried out at 300 K for 5 ps with a time step of 1 fs. AIMD simulations were performed for the pristine, single-Na-adsorbed, and Na-saturated configuration. The phonon dispersions of the pristine HfSTe monolayer were obtained from finite-displacement calculations on a 4 × 4 × 1 supercell using the PHONOPY package.[43] The diffusion energy barriers for Na migration were evaluated using the climbing-image nudged elastic band (CI-NEB) method,[44] as implemented in the VASP code.

3 Results and discussion

The fully optimized atomic structure of the Janus HfSTe monolayer is presented in Fig. 1(a). The material adopts a two-dimensional hexagonal lattice, in which the Hf atomic layer is asymmetrically sandwiched between S and Te layers, giving rise to a characteristic Janus configuration with broken out-of-plane mirror symmetry. The in-plane lattice constant is determined to be 3.78 Å, which is in good agreement with previously reported values by Lim *et al.* (3.80 Å)[34] and Shi *et al.* (3.79 Å).[21]

On the basis of the optimized structure, the electronic properties of the HfSTe monolayer are examined through its total band structure and projected band structure, as shown in Fig. 1(b). Several energy bands are observed to cross the Fermi level, indicating that the HfSTe monolayer exhibits an intrinsic metallic character. The electronic states near and above the Fermi level are predominantly contributed by the Hf 5d orbitals, whereas the Te 5p orbitals mainly contribute to the lower-energy regions below the Fermi level, as shown in Fig. 1(b). The intrinsic metallic nature of the Janus HfSTe monolayer is beneficial for electrode applications as it facilitates efficient electron transport during electrochemical processes.

Next, the mechanical response of the HfSTe monolayer is examined to evaluate its structural robustness. The in-plane elastic behavior, summarized in Fig. 2(a and b), reveals a circular angular dependence of the Young's modulus (75.1 N m^{-1}), confirming complete in-plane isotropy. The Poisson's ratio also remains direction-independent, with an value of 0.323, suggesting a stable elastic response under in-plane deformation. The calculated in-plane stiffness tensor yields C_{11} = 83.9 N m^{-1}, C_{12} = 27.1 N m^{-1}, and C_{66} = 28.3 N m^{-1}. These values satisfy the Born stability criteria for two-dimensional hexagonal crystals, namely $C_{11} > 0$ and $C_{11} > |C_{12}|$,[45] confirming the mechanical stability of the monolayer against small elastic deformations.

The thermal and dynamical stability of the HfSTe monolayer are further evaluated to ensure its structural integrity under finite-temperature conditions. AIMD simulations are carried out at temperature of 300 K for a duration of 5 ps. During the simulation, the temperature fluctuates around the target value, while the total energy remains stable without noticeable drift or abrupt changes, as depicted in Fig. 2(c). The final configuration does not exhibit bond breaking, structural reconstruction, or significant lattice distortion, indicating good thermal stability. Consistently, the phonon dispersion shown in Fig. 2(d) contains

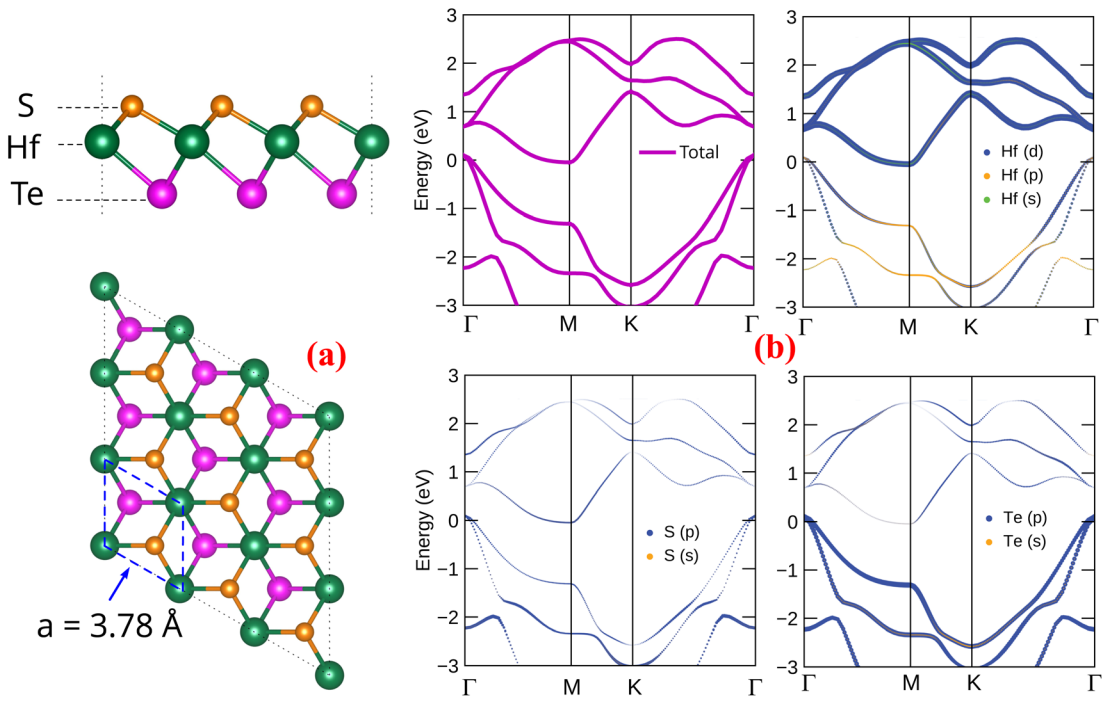

Fig. 1 (a) Side and top views of the crystal structure of the Janus HfSTe monolayer, (b) electronic band structure and projected orbital contributions of the HfSTe monolayer along the high-symmetry path Γ–M–K–Γ.

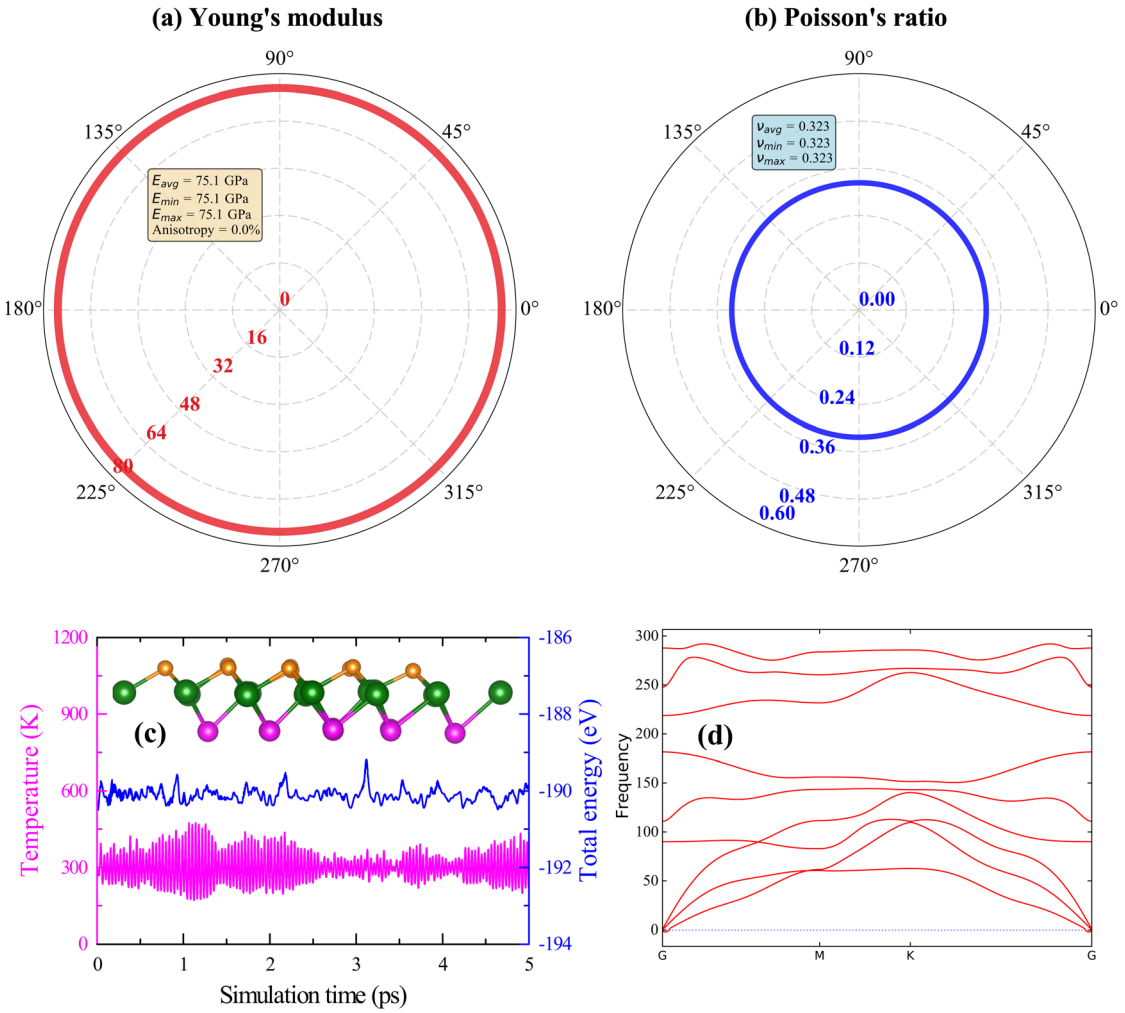

Fig. 2 In-plane angular variation of (a) Young's modulus (N m^{-1}) and (b) Poisson's ratio for the HfSTe monolayer. (c) Total energy and temperature profiles from AIMD simulations. (d) Phonon dispersion along the high-symmetry points in the Brillouin zone.

no imaginary modes throughout the Brillouin zone, confirming the dynamical stability of the HfSTe monolayer at the ground state. These results collectively suggest that the material possesses sufficient mechanical, thermal, and lattice-dynamical stability for further consideration in energy storage applications.

Based on the established structural stability and electronic properties, we next investigate Na adsorption on the Janus HfSTe monolayer. To elucidate the Na-ion storage behavior, Na atoms are adsorbed on the surface of the Janus HfSTe monolayer with progressively increasing coverage. Owing to the intrinsic Janus asymmetry, Na adsorption on the S-terminated and Te-terminated surfaces is examined separately. High-symmetry adsorption sites, including on-top, bridge, and hollow positions, on both surfaces of the 3 × 3 HfSTe supercell are illustrated in Fig. 3(a and b). All configurations were fully optimized, and the Na adsorption energy was evaluated according to

$$E_{ad} = E_{Na/HfSTe} - E_{HfSTe} - \mu_{Na}, \quad (1)$$

where $E_{Na/HfSTe}$, E_{HfSTe}, and μ_{Na} denote the total energies of the Na-adsorbed system, the pristine monolayer, and bulk Na per atom, respectively.

After identifying the most stable adsorption site within the central region of the supercell for each newly added Na atom, a complete Na layer is constructed by replicating the adsorbed Na atoms across the in-plane 3 × 3 lattice, corresponding to nine Na atoms per layer. The resulting full-layer configuration is then fully optimized. Subsequently, another Na atom is placed at different adsorption sites on both surfaces of the relaxed configuration, and geometry optimizations are performed again to determine the preferred adsorption site. This procedure is repeated iteratively until the Na adsorption energy becomes positive, thereby defining the Na-saturated adsorption configuration on the Janus HfSTe monolayer.

The adsorption energies corresponding to the stable configurations of the first Na atom on the HfSTe monolayer are summarized in Fig. 3(c). The results show that Na adsorption is significantly more favorable at hollow sites than at on-top sites, because the hollow geometry allows the adsorbed Na atom to interact more effectively with several neighboring substrate

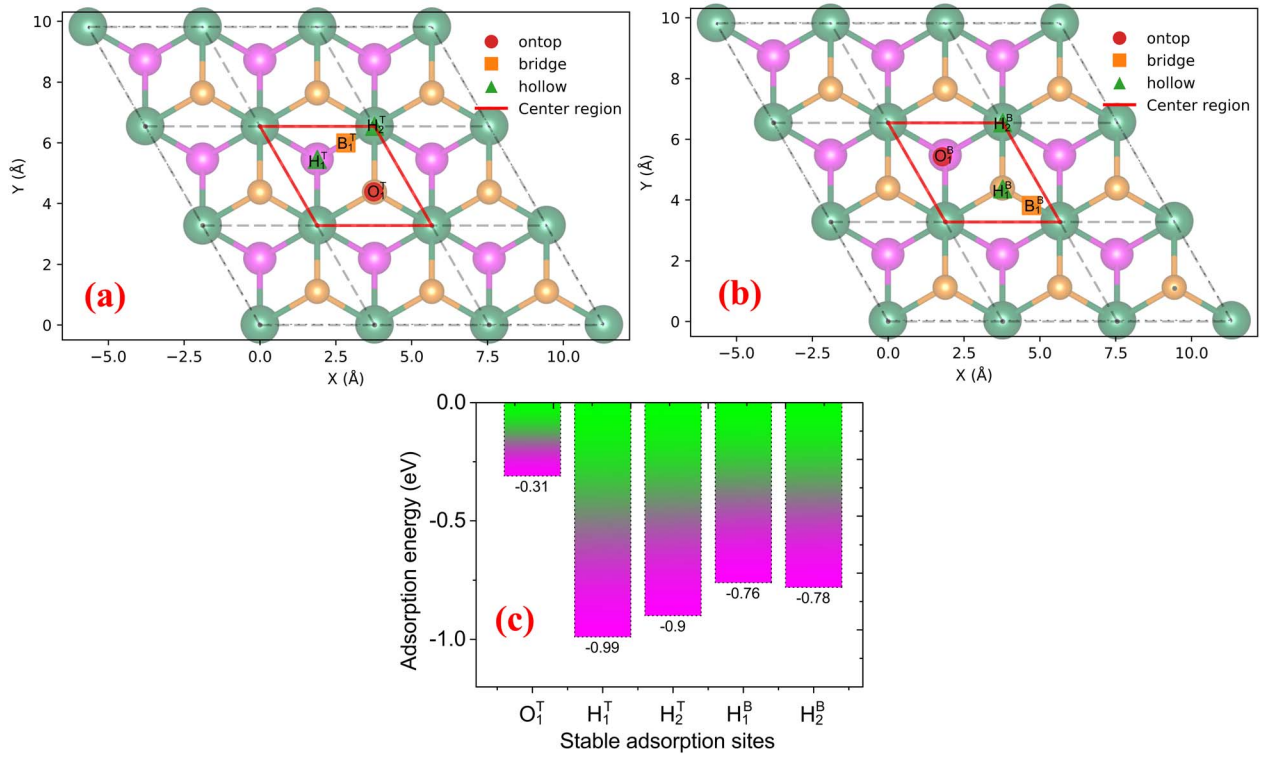

Fig. 3 Possible Na adsorption sites on the HfSTe monolayer: (a) top (S-terminated) surface, (b) bottom (Te-terminated) surface, and (c) Na adsorption energies at the most stable sites. Superscripts T and B denote the top and bottom surfaces, respectively; H, B, and O denote the hollow, bridge, and on-top sites.

atoms and thus provides more favorable local coordination. Notably, the S-terminated surface exhibits more negative adsorption energies than the Te-terminated surface, indicating a pronounced difference in chemical affinity between the two Janus surfaces. This behavior can be attributed to the higher electronegativity of S (2.58) compared with Te (2.10),[46] which leads to stronger ionic–electrostatic interactions between Na and the host lattice and therefore stronger Na binding on the S-terminated side. Among all the considered configurations, Na adsorption at the hollow H_1^T site on the S-terminated surface yields the most negative adsorption energy (−0.99 eV), which can be understood as the combined result of the favorable hollow-site coordination and the stronger adsorption affinity of the S-terminated surface. It is therefore identified as the most stable adsorption configuration among all the considered sites during the initial stage of sodiation.

To further elucidate the bonding nature and stabilization mechanism of the most favorable adsorption configuration, Fig. 4 presents the charge density difference (CDD), band structure, and DOS of the Na@HfSTe system corresponding to the H_1^T site. The CDD is employed to quantify the charge redistribution induced by Na adsorption and is defined as:

$$\Delta\rho = \rho_{\mathrm{HfSTe+Na}} - \rho_{\mathrm{HfSTe}} - \rho_{\mathrm{Na}}, \quad (2)$$

where the terms correspond to the charge densities of the adsorbed system, pristine HfSTe monolayer, and isolated Na atom, respectively.

As illustrated in Fig. 4(a), the CDD map exhibits a pronounced charge depletion around the Na atom accompanied by significant charge accumulation on the neighboring S atoms and, to a lesser extent, on the underlying Hf atoms. This distinct charge redistribution indicates that Na donates electrons to the HfSTe monolayer upon adsorption, consistent with

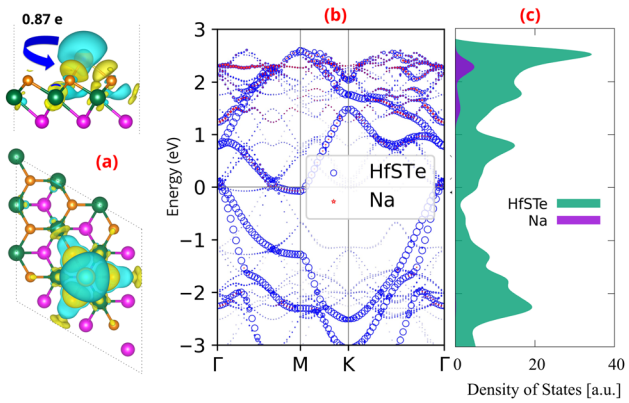

Fig. 4 (a) Charge density difference (CDD) map of Na adsorption at the hollow (H_1^T) site on the S-terminated surface of the Janus HfSTe monolayer; charge accumulation and depletion are indicated by yellow and blue regions, respectively (isosurface value: 0.001 e bohr^{-3}). (b) Electronic band structure and (c) projected density of states (PDOS) of the Na@HfSTe system, with contributions from the Na atom and the HfSTe substrate.

the commonly observed behavior of alkali-metal adsorption on two-dimensional materials.[47,48] Quantitative charge analysis shows that approximately 0.87*e* is transferred from Na to the host material, demonstrating a strong charge donation effect. This result is consistent with the large electronegativity difference between Na (0.93) and the S (2.58) atoms[46] in the Janus structure and further rationalizes why the hollow site on the S-terminated surface is energetically the most favorable adsorption site.

The band structure of the Na@HfSTe system shows that the metallic nature of the HfSTe monolayer is preserved after Na adsorption, with multiple bands crossing the Fermi level (Fig. 4(b)). The electronic states near the Fermi level are predominantly contributed by the HfSTe substrate, whereas the Na-related states are mainly distributed around and above the Fermi level. These results indicate that Na adsorption preserves the structural integrity of the host lattice without causing pronounced electron localization, thereby supporting efficient charge transport. This conclusion is further supported by the total DOS shown in Fig. 4(c), where a high DOS at the Fermi level is maintained after Na adsorption, indicates that the electrical conductivity of the HfSTe monolayer is not degraded during the initial sodiation process.

Having identified H_1^T as the most stable adsorption configuration with strong charge transfer, AIMD simulations at 300 K for 5 ps further support the thermal stability of this representative single-Na adsorption state, as shown in Fig. S1 of the SI. We next evaluate the Na-ion transport kinetics on the S-terminated surface. The possible Na-ion migration pathways were constructed from the adsorption-site network centered on the most stable H_1^T sites. In the 3 × 3 supercell, three geometrically distinct candidate H_1^T-to-H_1^T routes can be identified, as shown in Fig. S2 of the SI: pathway 1, $H_1^T \rightarrow H_2^T \rightarrow H_1^T$, *via* an intermediate H_2^T hollow site; pathway 2, a direct $H_1^T \rightarrow H_1^T$ hop at about 30° with respect to the *a*-axis; and pathway 3, a direct $H_1^T \rightarrow H_1^T$ hop parallel to the *a*-axis. During CI–NEB optimization, pathway 3 relaxes onto a trajectory equivalent to pathway 1. Therefore, only two representative non-equivalent pathways were retained for comparison.

For diffusion pathway 1 (Fig. 5(a)), Na migrates between two neighboring H_1^T hollow sites through an intermediate configuration close to the H_2^T hollow site. The maximum barrier along this route is about 0.18 eV, indicating a kinetically favorable diffusion process. The energy profile exhibits two local maxima separated by an intermediate minimum, suggesting a stepwise adjustment of the Na coordination environment with surrounding S and Hf atoms during migration. In contrast, diffusion pathway 2 (Fig. 5(b)) shows a substantially higher barrier, with the main maximum reaching 0.68 eV. Along this direct migration route, Na passes through a less favorable coordination region, where the Na-surface interaction becomes weaker, leading to a larger activation penalty.

The lower barrier of pathway 1 can therefore be attributed to the smoother variation of the Na-surface interaction along this route. Since the transition-state region remains close to a favorable hollow coordination environment, the adsorption-energy penalty relative to the H_1^T minimum is smaller than that of pathway 2. This interpretation is consistent with previous studies showing that ion migration barriers on 2D anode materials are strongly influenced by the relative adsorption-energy difference between stable and intermediate sites along the diffusion path, rather than solely by the absolute adsorption energy at the most stable site.[49]

A comparison of the two diffusion pathways indicates that pathway 1 is kinetically more favorable and is therefore expected to serve as the preferred Na-ion diffusion channel on the S-terminated surface of the Janus HfSTe monolayer. The corresponding Na-ion diffusion barrier is calculated to be 0.18 eV, placing HfSTe among 2D anode materials with relatively low Na-ion diffusion barriers. Although this value is higher than those of several previously reported Janus monolayers, such as WSSe (0.07 eV),[28] MoSSe (0.075 eV),[29] TiSSe (0.11 eV),[50] and VSSe (0.10 eV),[51] it remains smaller than that of many other representative 2D materials, including monolayer black phosphorus (0.35 eV),[52] silicene (0.25 eV),[53] and graphene (0.19 eV).[54] Overall, the 0.18 eV barrier of HfSTe, while moderate among Janus monolayers, suggests favorable Na-ion transport kinetics for sodium-ion battery anode applications.

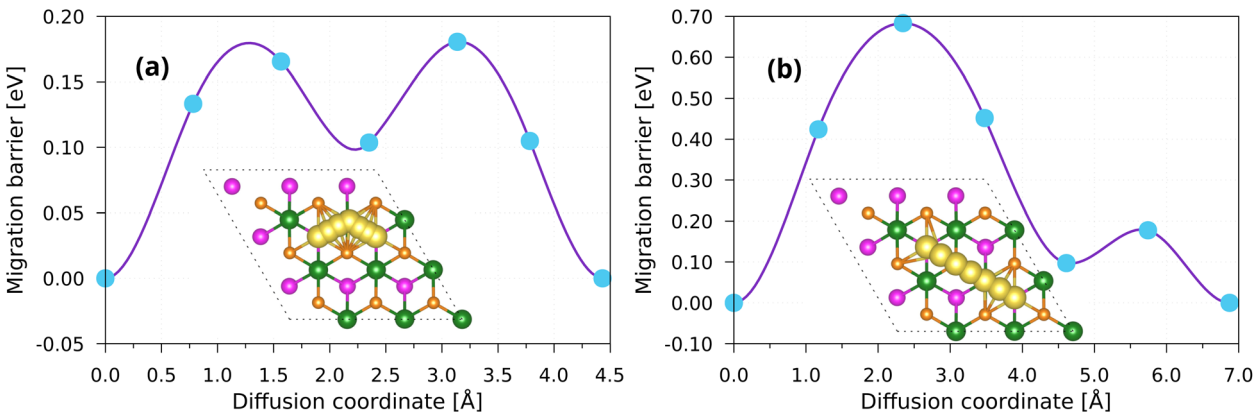

Fig. 5 Diffusion energy barriers of Na on the S-terminated surface of the Janus HfSTe monolayer: (a) pathway 1 describing Na migration between adjacent most stable hollow sites along the lattice-edge direction, and (b) pathway 2 describing Na migration between equivalent hollow sites along the diagonal direction, calculated using the CI-NEB method.

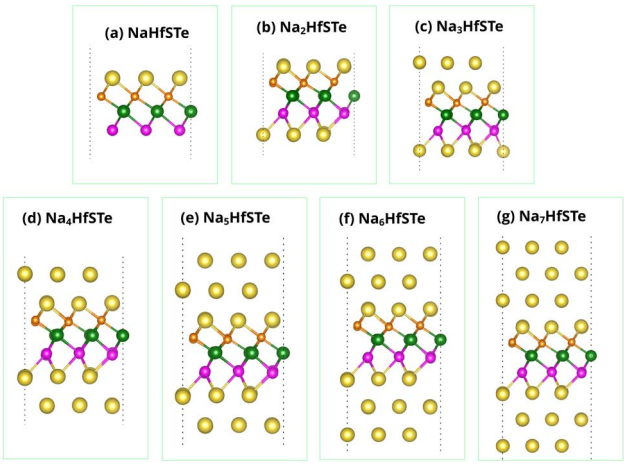

Fig. 6 Top and side views of representative Na_xHfSTe configurations: (a) $x = 1$, (b) $x = 2$, (c) $x = 3$, (d) $x = 4$, (e) $x = 5$, (f) $x = 6$, and (g) $x = 7$, illustrating the evolution of Na adsorption from surface-bound sites to multilayer Na accumulation. Each configuration is labeled with its average Na adsorption energy (eV).

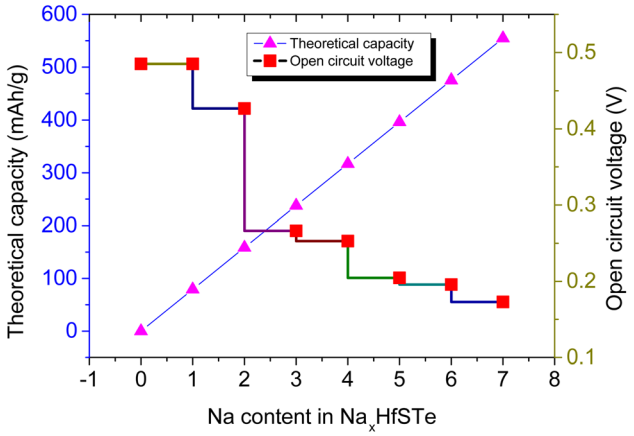

Fig. 7 Calculated open-circuit voltage of Na_xHfSTe as a function of x, illustrating the voltage evolution during progressive sodiation.

We further investigate the Na intercalation behavior of the HfSTe monolayer under progressive sodiation. The optimized adsorption configurations for Na coverages ranging from $x = 1$ to 7 are shown in Fig. 6, illustrating the evolution of the Na arrangement with increasing Na concentration. It is found that the average adsorption energy of Na remains negative throughout the entire sodiation range considered, indicating that the sodiation process is energetically favorable at all Na coverages. Meanwhile, no obvious structural collapse or reconstruction is observed in the HfSTe monolayer at any Na coverage, suggesting that the Janus framework can robustly accommodate progressive Na insertion. To further assess the structural integrity under realistic conditions, AIMD simulations at 300 K were performed for the saturated Na-adsorbed configuration ($x = 7$) (Fig. S3, SI). The results show that the HfSTe framework remains intact without obvious Na clustering, confirming the thermal stability of the highly sodiated structure.

The open-circuit voltage (OCV) between two adjacent sodiation states is evaluated according to:

$$V = -\frac{E(\mathrm{Na}_{x_2}\mathrm{HfSTe}) - E(\mathrm{Na}_{x_1}\mathrm{HfSTe}) - (x_2 - x_1)E_{\mathrm{Na}}}{(x_2 - x_1)e}, \quad (3)$$

Within this definition, a negative Na-insertion energy corresponds to a positive voltage, indicating thermodynamically favorable Na adsorption.

Fig. 7 presents the calculated OCV profile of the Na_xHfSTe system as a function of Na concentration, providing insight into the electrochemical behavior during progressive sodiation. At low Na concentrations ($x = 1$ and 2), Na atoms favor the energetically preferred hollow sites on the S- and Te-terminated surfaces, resulting in strong Na–substrate interactions and relatively high OCV values. With further Na insertion ($x \geq 3$), the favorable adsorption sites gradually become saturated and additional Na atoms are accommodated at less favorable or higher-lying positions. Consequently, the adsorption strength weakens due to enhanced Na–Na repulsive interactions, resulting in a gradual decrease in OCV for $x = 3$–7, within the low-voltage window desirable for anode materials. Notably, the OCV remains positive throughout the entire sodiation range, confirming the thermodynamic feasibility of Na storage in the HfSTe monolayer even at deep sodiation levels.

The theoretical specific capacity of Janus HfSTe was estimated from:

$$C = \frac{n_{\max} z F}{M}, \quad (4)$$

where $n_{\max} = 7$ is the maximum Na storage capacity per HfSTe unit cell, $z = 1$ is the valence of Na^+, $F = 26\,801$ mAh mol^{-1} is the Faraday constant, and M is the molar mass of the pristine HfSTe monolayer.

The theoretical specific capacity of the Janus HfSTe monolayer is calculated to be 554.8 mAh g^{-1}. This value is lower than those of some Janus-type monolayers with exceptionally high Na-storage capacities, such as V_2COS (663 mAh g^{-1}),[55] BeSeCl (699 mAh g^{-1}),[31] and MoPC (1157.46 mAh g^{-1}).[56] In contrast, the capacity of the HfSTe monolayer exceeds or matches that of several representative Janus monolayers for Na storage, including MoSSe (510 mAh g^{-1}),[29] TiSSe (337 mAh g^{-1}),[50] and VSSe (331 mAh g^{-1}).[51] It also significantly exceeds that of WSSe (371.5 mAh g^{-1}).[28] A comprehensive comparison of key electrochemical properties of the HfSTe monolayer with those of recently reported Janus anode materials, including electronic characteristics, average open-circuit voltage, theoretical capacity, and Na-ion diffusion barrier, is summarized in Table 1. Overall, the Janus HfSTe monolayer exhibits a well-balanced electrochemical performance by combining a relatively high specific capacity, low average OCV, intrinsic metallic conductivity, and a low Na-ion diffusion barrier, highlighting its potential as a competitive anode material for SIBs.

To further evaluate the electronic robustness of the HfSTe monolayer under deep sodiation, Fig. 8 presents the density of states for the two highest Na concentrations considered, namely Na_6HfSTe and Na_7HfSTe. In both cases, the Fermi level

Table 1 Comparison of electrochemical properties of the HfSTe monolayer with representative 2D Janus anode materials for SIBs

Material	Conductivity/phase transition	C_{max} (mAh g^{-1})	OCV_{avg} (V)	E_{diff}^{min} (eV)	Ref.
HfSTe	Metallic	554.8	0.33	0.18	This work
WSSe	Semiconductor → metallic	371.5	0.57	0.04	28
MoSSe	—	510	—	0.075	29
TiSSe	—	337	0.15	0.104	50
VSSe	—	331	0.72	0.10	51
V_2COS	—	663	0.76	0.12	55
BeSeCl	Metallic	699	0.91	0.08	31

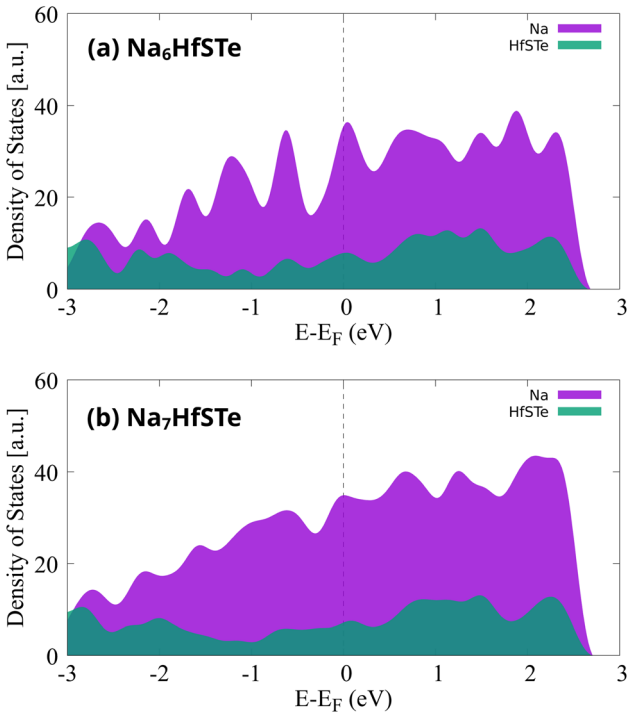

Fig. 8 PDOS of the Janus HfSTe monolayer at high Na coverage: (a) Na_6HfSTe and (b) Na_7HfSTe. Projected contributions from the HfSTe host and Na are shown, highlighting the preservation of metallic character under deep sodiation.

intersects a continuous distribution of electronic states, confirming that the systems retain their metallic character even at high Na content. Electronic states around the Fermi level are primarily dominated by the adsorbed Na atoms (purple region), while the HfSTe host (green region) plays a secondary role. This feature suggests that Na incorporation not only maintains but further improves the electronic conductivity of the sodiated system. The retained metallic character facilitates rapid electron transfer during cycling, a key factor for high-performance anode materials.

Finally, to better understand the structural response of the HfSTe monolayer to Na insertion, we quantified the deformation of the host lattice by tracking the geometric changes in the HfSTe framework across different Na adsorption concentrations. Because the in-plane lattice parameters (a and b) exhibit negligible variation during sodiation, the structural change of the host can be effectively characterized through the variation in its out-of-plane thickness. The corresponding relative expansion is defined as:

$$\varepsilon = \frac{t - t_0}{t_0} \times 100\%, \quad (5)$$

where t_0 is the thickness of the pristine HfSTe monolayer and t denotes the thickness of the HfSTe framework at a given Na concentration.

As illustrated in Fig. 9(a and b), the calculated thickness expansion of the host layer varies from approximately 3.3% at low Na coverage to a maximum of 10.55% at high sodiation. Notably, even under the largest deformation conditions, the HfSTe lattice preserves its structural integrity without noticeable bond breaking or framework collapse. This limited dimensional change suggests that the Janus HfSTe monolayer possesses sufficient mechanical adaptability to accommodate Na insertion and extraction. Such structural robustness is

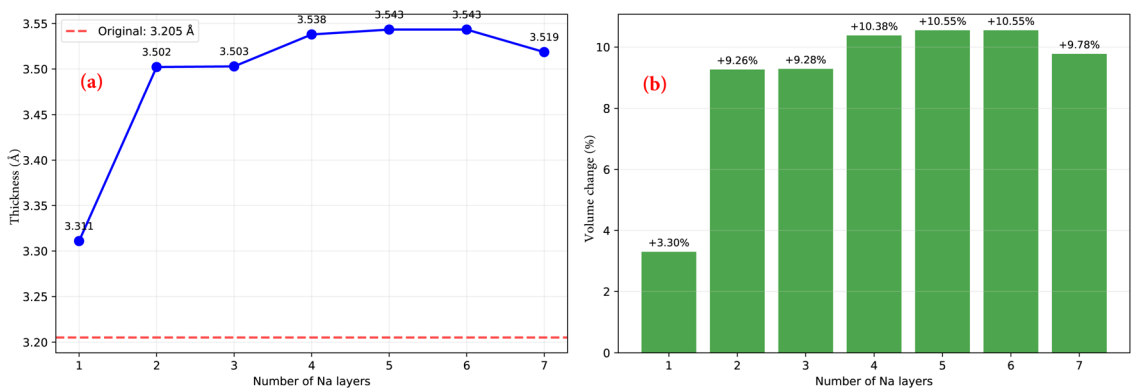

Fig. 9 (a) Thickness variation and (b) relative volume change of the Janus HfSTe monolayer upon Na storage at different Na contents.

advantageous for ensuring reversible ion storage and sustaining stable cycling behavior over prolonged electrochemical operation.

4 Conclusion

In summary, a systematic first-principles study has been performed to evaluate the Janus HfSTe monolayer as a sodium-ion battery anode. The pristine HfSTe monolayer exhibits intrinsic metallic behavior and good mechanical, thermal, and dynamical stability. Owing to the Janus asymmetry, Na adsorption is surface-dependent and energetically favored at hollow sites on the S-terminated surface, accompanied by substantial charge transfer. CI-NEB calculations reveal a low Na diffusion barrier of 0.18 eV *via* the preferred migration pathway, indicating favorable ion-transport kinetics. With increasing Na concentration, Na is stored *via* a layer-by-layer adsorption mechanism, leading to a high theoretical capacity of 554.8 mAh g^{-1} and an average open-circuit voltage of about 0.33 V. Notably, HfSTe retains its metallic character even at high sodiation levels, accompanied by a moderate volume change. These results suggest that the Janus HfSTe monolayer is a viable anode candidate for sodium-ion batteries, combining high Na-storage capacity, fast ion-transport kinetics, and structural robustness.

Conflicts of interest

There are no conflicts of interest to declare.

Data availability

The data supporting this article are available in the supplementary information (SI). Supplementary information: the convergence tests, AIMD simulations of the single-Na-adsorbed, and Na-saturated HfSTe systems, the possible Na-ion diffusion pathways, and the optimized structure of the pristine 1T-HfSTe monolayer. See DOI: https://doi.org/10.1039/d6na00120c.

References

1 T. Kim, W. Song, D.-Y. Son, L. K. Ono and Y. Qi, *J. Mater. Chem. A*, 2019, **7**, 2942–2964.
2 C. Grosjean, P. H. Miranda, M. Perrin and P. Poggi, *Renewable Sustainable Energy Rev.*, 2012, **16**, 1735–1744.
3 M. Li, J. Lu, Z. Chen and K. Amine, *Adv. Mater.*, 2018, **30**, 1800561.
4 H. Lim, J. Sung, J.-W. Jung and W. Choi, *Chem. Commun.*, 2025, **61**, 16150–16169.
5 M. Fleming, S. G. Kannan and R. Eggert, *Resour. Policy*, 2024, **97**, 105226.
6 Z. He, Y. Huang, H. Liu, Z. Geng, Y. Li, S. Li, W. Deng, G. Zou, H. Hou and X. Ji, *Nano Energy*, 2024, **129**, 109996.
7 J. C. Barbosa, R. S. Pinto, J. P. Serra, C. M. Costa, S. Lanceros-Mendez and R. Gonçalves, *J. Mater. Chem. A*, 2025, **13**, 35952–35975.
8 T. Perveen, M. Siddiq, N. Shahzad, R. Ihsan, A. Ahmad and M. I. Shahzad, *Renewable Sustainable Energy Rev.*, 2020, **119**, 109549.
9 Z. Zhu, T. Jiang, M. Ali, Y. Meng, Y. Jin, Y. Cui and W. Chen, *Chem. Rev.*, 2022, **122**, 16610–16751.
10 P.-C. Tsai, S.-C. Chung, S.-K. Lin and A. Yamada, *J. Mater. Chem. A*, 2015, **3**, 9763–9768.
11 P. Ge and M. Fouletier, *Solid State Ionics*, 1988, **28**, 1172–1175.
12 Y. Wan, B. Huang, W. Liu, D. Chao, Y. Wang and W. Li, *Adv. Mater.*, 2024, **36**, 2404574.
13 L. Li, Y. Zheng, S. Zhang, J. Yang, Z. Shao and Z. Guo, *Energy Environ. Sci.*, 2018, **11**, 2310–2340.
14 A. Shivannanaik, A. Balighatta Rameshkumar, Udayabhanu and P. Kalappa, *Crit. Rev. Solid State Mater. Sci.*, 2025, **50**, 296–320.
15 M. Yuan, X. Zheng, J. Xu, Q. Ni, L. Luo, Z. Cai, Z. Sun, L. Lin and G. Sun, *Batteries*, 2023, **9**, 48.
16 S. Saharan and S. Meena, *J. Electrochem. Soc.*, 2025, **172**, 100530.
17 A.-Y. Lu, H. Zhu, J. Xiao, C.-P. Chuu, Y. Han, M.-H. Chiu, C.-C. Cheng, C.-W. Yang, K.-H. Wei, Y. Yang, *et al.*, *Nat. Nanotechnol.*, 2017, **12**, 744–749.
18 W.-J. Yin, H.-J. Tan, P.-J. Ding, B. Wen, X.-B. Li, G. Teobaldi and L.-M. Liu, *Mater. Adv.*, 2021, **2**, 7543–7558.
19 L. Zhang, Y. Xia, X. Li, L. Li, X. Fu, J. Cheng and R. Pan, *J. Appl. Phys.*, 2022, **131**, 230902.
20 R. Li, Y. Cheng and W. Huang, *Small*, 2018, **14**, 1802091.
21 W. Shi and Z. Wang, *J. Phys.: Condens. Matter*, 2018, **30**, 215301.
22 X. Zheng, Y. Zhou and Y. Guo, *Acc. Mater. Res.*, 2024, **6**, 124–128.
23 J. Zhang, S. Jia, I. Kholmanov, L. Dong, D. Er, W. Chen, H. Guo, Z. Jin, V. B. Shenoy, L. Shi, *et al.*, *ACS Nano*, 2017, **11**, 8192–8198.
24 S. Lakshmy, B. Mondal, N. Kalarikkal, C. S. Rout and B. Chakraborty, *Adv. Powder Mater.*, 2024, **3**, 100204.
25 S. Tao, B. Xu, J. Shi, S. Zhong, X. Lei, G. Liu and M. Wu, *J. Phys. Chem. C*, 2019, **123**, 9059–9065.
26 G. Chaney, A. Ibrahim, F. Ersan, D. Çakır and C. Ataca, *ACS Appl. Mater. Interfaces*, 2021, **13**, 36388–36406.
27 C. Shang, X. Lei, B. Hou, M. Wu, B. Xu, G. Liu and C. Ouyang, *J. Phys. Chem. C*, 2018, **122**, 23899–23909.
28 S. Ahmad, H. Din, S. Nawaz, S.-T. Nguyen, C. Q. Nguyen and C. V. Nguyen, *Appl. Surf. Sci.*, 2023, **632**, 157545.
29 H. Wang, Q. Chen, H. Li, Q. Duan, D. Jiang and J. Hou, *Chem. Phys. Lett.*, 2019, **735**, 136777.
30 T. V. Vu, D.-Q. Hoang, T. H. Ho, H. Van Chi and K. D. Pham, *Nanoscale Adv.*, 2026, **8**, 673–681.
31 N. Verma and A. Kumar, *J. Mater. Chem. A*, 2025, **13**, 28559–28573.
32 A. Bouheddadj, A. Daouli, T. Ouahrani, R. Boufatah and M. Badawi, *Mater. Chem. Phys.*, 2022, **289**, 126489.
33 M. Barhoumi, K. Lazaar, W. Dimassi and M. Said, *Results Chem.*, 2026, **25**, 103266.

34 H. L. C. Lim, E. T. Tobias, G.-Y. Chen, Y.-L. Lu, A. B. Santos-Putungan, A. A. B. Padama, S.-H. Lin and D. B. Putungan, *2D Mater.*, 2024, **11**, 045018.
35 T. Choudhary, S. Vinod and R. K. Biswas, *Phys. Chem. Chem. Phys.*, 2026, **28**, 5288–5302.
36 G. Kresse and J. Furthmüller, *Phys. Rev. B: Condens. Matter Mater. Phys.*, 1996, **54**, 11169–11186.
37 G. Kresse and J. Furthmüller, *Comput. Mater. Sci.*, 1996, **6**, 15–50.
38 S. Grimme, S. Ehrlich and L. Goerigk, *J. Comput. Chem.*, 2011, **32**, 1456–1465.
39 H. J. Monkhorst and J. D. Pack, *Phys. Rev. B*, 1976, **13**, 5188.
40 V. Wang, N. Xu, J.-C. Liu, G. Tang and W.-T. Geng, *Comput. Phys. Commun.*, 2021, **267**, 108033.
41 S. Nosé, *Mol. Phys.*, 1984, **52**, 255–268.
42 W. G. Hoover, *Phys. Rev. A*, 1985, **31**, 1695.
43 A. Togo, L. Chaput and I. Tanaka, *Phys. Rev. B: Condens. Matter Mater. Phys.*, 2015, **91**, 094306.
44 G. Henkelman, B. P. Uberuaga and H. Jónsson, *J. Chem. Phys.*, 2000, **113**, 9901–9904.
45 M. Born and K. Huang, *Dynamical Theory of Crystal Lattices*, Oxford university press, 1996.
46 T. L. Brown, H. E. LeMay, B. E. Bursten and L. S. Brunauer, *Chemistry: the Central Science*, Prentice Hall, Englewood Cliffs, NJ, 1997, vol. 13.
47 H. Sahin and F. M. Peeters, *Phys. Rev. B: Condens. Matter Mater. Phys.*, 2013, **87**, 085423.
48 S. Yang, S. Li, S. Tang, W. Dong, W. Sun, D. Shen and M. Wang, *Theor. Chem. Acc.*, 2016, **135**, 164.
49 S. Banerjee, A. Narwal, S. K. Reddy and S. S. Yamijala, *Phys. Chem. Chem. Phys.*, 2023, **25**, 11789–11804.
50 O. Al-Qurashi, K. A. Soliman, H. Lgaz, Z. Safi and N. Wazzan, *J. Mol. Model.*, 2024, **30**, 405.
51 F. Xiong and Y. Chen, *Nanotechnology*, 2020, **32**, 025702.
52 Y. Xu, Y. Fu, X. Gong, J. Xu and W. Liu, *Mater. Today Commun.*, 2024, **41**, 110394.
53 X.-X. Guo, P. Guo, J.-M. Zheng, L.-K. Cao and P.-J. Zhao, *Appl. Surf. Sci.*, 2015, **341**, 69–74.
54 X. Sun, Z. Wang and Y. Q. Fu, *Carbon*, 2017, **116**, 415–421.
55 F. Wang, J. Yuan, Z. Zhang, B. Song, J. Zhao, J. Yue, T. Xu and J. Zhou, *Phys. Rev. Mater.*, 2024, **8**, 085801.
56 T. V. Vu, D.-Q. Hoang, T. H. Ho, H. D. Tong and K. D. Pham, *RSC Adv.*, 2026, **16**, 14951–14958.

